

PAPER • OPEN ACCESS

# Improvement in the simulation tools for heat distribution predictions and control of baffle and middle divertor loads in Wendelstein 7-X

To cite this article: Yu Gao *et al* 2023 *Nucl. Fusion* **63** 026031

View the [article online](#) for updates and enhancements.

## You may also like

- [Development of a synthetic phase contrast imaging diagnostic for turbulence studies at Wendelstein 7-X](#)  
S K Hansen, M Porkolab, J-P Böhner *et al.*
- [W7-X and the sawtooth instability: towards realistic simulations of current-driven magnetic reconnection](#)  
Alessandro Zocco, Alexey Mishchenko, Carolin Nührenberg *et al.*
- [Plasma–surface interaction in the stellarator W7-X: conclusions drawn from operation with graphite plasma-facing components](#)  
S. Breznsek, C.P. Dhard, M. Jakubowski *et al.*

# Improvement in the simulation tools for heat distribution predictions and control of baffle and middle divertor loads in Wendelstein 7-X

Yu Gao<sup>1,\*</sup> , Yuhe Feng<sup>1</sup> , Michael Endler<sup>1</sup> , Marcin W. Jakubowski<sup>1</sup> , Joachim Geiger<sup>1</sup>, Sergey Bozhenkov<sup>1</sup> , Aleix Puig Sitjes<sup>1</sup>, Fabio Pisano<sup>2</sup> , Chandra Prakash Dhard<sup>1</sup>, Dirk Naujoks<sup>1</sup>, Maciej Krychowiak<sup>1</sup>, Matthias Otte<sup>1</sup>, Ralf König<sup>1</sup>, Daihong Zhang<sup>1</sup> , Georg Schlisio<sup>1</sup> , Uwe Wenzel<sup>1</sup> , Thomas Sunn Pedersen<sup>1</sup>  and the W7-X Team<sup>1,a</sup>

<sup>1</sup> Max-Planck-Institut für Plasmaphysik, 17491 Greifswald, Germany

<sup>2</sup> Department of Electrical and Electronic Engineering, University of Cagliari, 09123 Cagliari, Italy

E-mail: [yu.gao@ipp.mpg.de](mailto:yu.gao@ipp.mpg.de)

Received 20 September 2022, revised 19 December 2022

Accepted for publication 29 December 2022

Published 17 January 2023



## Abstract

In the first divertor campaign in Wendelstein 7-X (W7-X), unexpected significant heat loads were observed at particular plasma-facing components (e.g. baffle tiles and middle divertor part) which were not designed to receive high heat flux. In a prior investigation, it was concluded that the previous diffusive field line tracing (DFLT) model used for divertor design in W7-X cannot reproduce these loads, due to the missing physics in simulating the heat transport in the shaded flux tubes. To tackle this issue, two new efficient codes (DFLT\_rev and EMC3-Lite) are introduced and validated against various experimental heat distributions in different magnetic configurations. The new tungsten baffle tiles have been designed with these codes and mounted in the machine, aiming for mitigated heat loads in the upcoming campaign.

Keywords: W7-X, EMC3-Lite, heat loads, simulation

(Some figures may appear in colour only in the online journal)

## 1. Introduction

The island divertor concept, firstly tested in W7-AS [1], has been successfully demonstrated in the first divertor campaign in Wendelstein 7-X (W7-X) equipped with ten inertially

cooled fine-grain graphite test divertor units (TDUs) [2–5]. These TDUs are distributed in a five-fold toroidal and an up-down flip symmetry in W7-X, aiming at sufficient power and particle exhausts [6, figure 1 therein]. Stable thermal detachment on all the TDUs was achieved in the previous campaign [7–11], and will be further explored in the upcoming experimental campaign with the newly installed water-cooled high-heat-flux (HHF) divertor and with a cryogenic pumping system.

However, in attached condition the operational regime was mainly limited by the overloads on the baffle tiles [12] or the middle divertor part instead of the predicted high-loaded area [13] (low-iota part, high-iota tail, and vertical target) of the divertor. The allowed steady-state maximum heat flux on

<sup>a</sup> See Sunn Pedersen *et al* 2022 (<https://doi.org/10.1088/1741-4326/ac2cf5>) for the W7-X Team.

\* Author to whom any correspondence should be addressed.



Original Content from this work may be used under the terms of the [Creative Commons Attribution 4.0 licence](https://creativecommons.org/licenses/by/4.0/). Any further distribution of this work must maintain attribution to the author(s) and the title of the work, journal citation and DOI.

the baffle tiles is  $0.5 \text{ MW m}^{-2}$ , and on the middle divertor part  $1 \text{ MW m}^{-2}$ , mainly determined by the upper thermal limit allowed for the CuCrZr heat sink of  $\sim 450 \text{ }^\circ\text{C}$  [14].

In W7-X, the main heat channel refers to the flux tube close to the separatrix containing open field lines with a wall-to-wall connection length  $L_c$  of hundreds of meters, which typically forms the outer boundary of the edge magnetic island. During the design phase of the W7-X divertor, the baffle and middle divertor components were optimized to be shaded by the divertor plates [13]. Specifically, no intersections with the main heat channel can be found on these components.

Nevertheless, plasma can enter the shadowed region radially through perpendicular transport from the vicinity of the main heat channel and transport along the flux tubes inside the shadowed region towards these components [12, 15]. The heat transport in the shadowed region was investigated in detail in [12]. The bidirectional heat transport was confirmed by the observation of overloads at the baffle tiles.

It has also been pointed out that the diffusive field line tracing (DFLT) [16], as the main tool used for heat flux distribution predictions throughout the divertor design phase of W7-X, can not reproduce the experimentally observed baffle loads, due to the incapability in simulating the bidirectional heat transport in the shadowed flux tubes. In contrast, EMC3-Eirene [17, 18] applying sheath boundary condition obtained good agreement with the experimental result regarding the baffle load [12].

An anisotropic diffusion model has been developed recently to mimic the physics of bidirectional heat transport [19]. In this new development, the proxy of diffusion is not only implemented in the perpendicular plane, but also in parallel to the magnetic field lines through a random walk process. Better simulation results are achieved with regards to the loads in the shadowed region, but with a price of a much longer calculation time by a factor of  $\sim 32$  compared to DFLT according to the paper. Both anisotropic diffusion and the complete EMC3-Eirene codes appear to be too slow to deliver heat distribution results in large quantities, which is one of the first steps for divertor optimization in stellarators with a variety of magnetic configurations as in W7-X.

This paper has three aims: (a) to present in section 2 an improved DFLT, namely DFLT\_rev method and a new EMC3-Lite [20] code for simulating the heat distributions, with both now considering the bidirectional heat transport in the shadowed flux tubes. (b) To document in section 3 different magnetic topology effects on the baffle and middle divertor loads and to validate the EMC3-Lite code by comparing with these experiments. (c) To show in section 4 the newly installed tungsten baffle tiles for the next campaign aiming at reduced baffle heat loads. Such an overview of the baffle and middle divertor loads is necessary for the preparation of the upcoming campaign regarding ways to mitigate them for machine safety. The confidence gained in EMC3-Lite through comparing with experiments also supports its use for future divertor optimization.

## 2. Heat distribution simulations with DFLT\_rev and EMC3-Lite

For divertor design and optimization in stellarators, fast and accurate tools are required for the estimation of heat distributions on PFCs. DFLT is commonly used for predicting the heat fluxes on the PFCs in W7-X thanks to the well-implemented web-service interfaces [16]. However, this model failed to predict the experimentally observed baffle loads [12], due to the missing physics in the shadowed region. In this section, the numerical implementation of DFLT will be re-examined and an improved DFLT\_rev model will be introduced to account for the bidirectional heat transport in the flux tubes. Heat flux simulation results from DFLT, DFLT\_rev, and EMC3-Lite will be quantitatively compared followed by a discussion on their advantages and limitations.

### 2.1. DFLT\_rev: reversed tracing step added to the DFLT

The web-service-based DFLT code [16] originated from the idea proposed in [21], in which diffusive broadening of the heat transport channel is approximated by Monte-Carlo perpendicular displacements implemented alongside the parallel tracing steps. Test particles are initially set up within the vicinity but inside the last closed flux surface (LCFS). They are diffusively traced along the field lines until the intersections with the PFCs, where heat fluxes can be derived from calculating the density of particles deposited within the predefined surface grids.

In DFLT, the perpendicular displacement happens after a random parallel tracing length  $x$  with a probability density distribution:  $p(x) = \lambda^{-1} \exp(-x/\lambda)$ . The direction of the displacement is random in the plane perpendicular to the local field line. The displacement distance  $r$  is distributed uniformly within the interval  $[0, \sqrt{12D_\perp \lambda / v_\parallel}]$ . The mean free path  $\lambda$  used for W7-X modeling is typically fixed to 0.1 m. A maximum tracing distance can be set in DFLT (10 km as a default value for W7-X) to stop the tracing of a possible test particle, which theoretically can jump in and out near the LCFS infinitely. The magnitude of the diffusion process is controlled solely by the ratio between the perpendicular particle diffusion coefficient  $D_\perp$  and the parallel flow velocity  $v_\parallel$ , i.e.  $D_\perp / v_\parallel$ , which is also named as ‘magnetic diffusivity’ [22, 23]. Due to the simplicity of the DFLT model, caution should be used when assigning physical significance to these values.

In DFLT, there is no possibility to reverse the parallel tracing direction after the test particles are launched. The predefined parallel flow direction are kept throughout the entire lifetime of the test particles traced from the LCFS until the PFCs. To mimic the counter-streaming flows in the island outside the LCFS [24], test particles are always launched twice, including one forward and one backward tracing with respect to the positive magnetic field direction (anticlockwise when viewing from the top in W7-X). Although such an approach seems to be valid for the main heat channel surrounding the

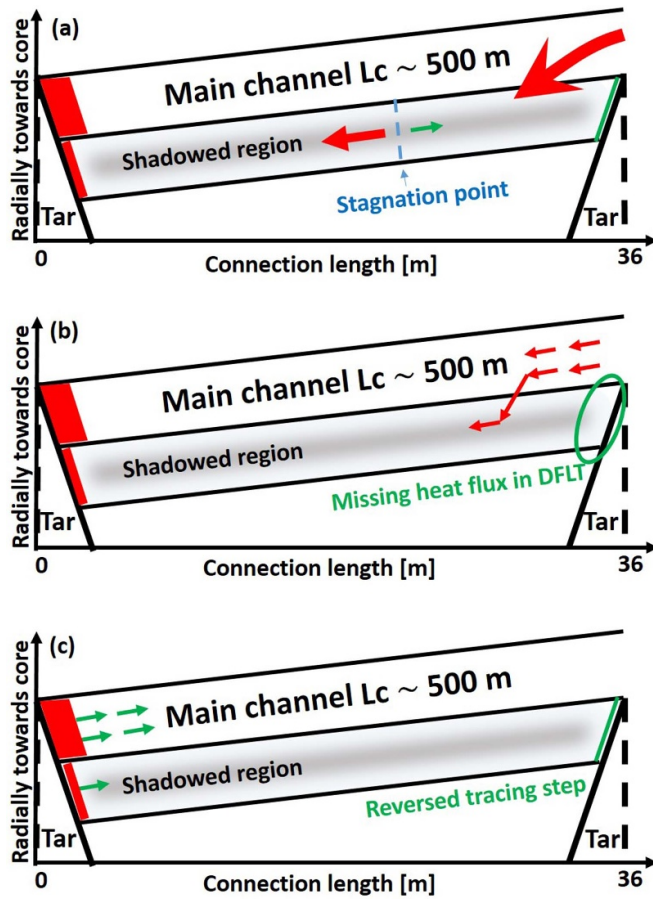


**Figure 1.** Schematic diagrams explaining heat transport in the shadowed region. (a) The physics picture of heat transport considering momentum exchange, e.g. the backflow to the right target in the shadowed region was reduced by friction against the main channel. (b) Illustration of the DFLT method, where energy-carrying particles are traced to approximate heat transport. Constant parallel flow direction in the code causes the missing heat flux to the right target. (c) The proposed additional reversed tracing step in DFLT\_rev. Deposited particles resulting from DFLT are traced inversely away from the PFCs.

island boundary, it cannot approximate the backflow in the shadowed region [12, 15].

The physics picture of heat transport, especially in the shadowed region at the very downstream can be explained in figure 1(a). Driven by sheath boundary condition and plasma pressure gradient, heat diffusing into certain flux tube should transport towards both ends of the tube through conduction and/or convection [25]. Only  $\sim 36$  m away from the left target, the part of the main heat channel being investigated is at a very downstream end, in which power flows universally towards the left target. Through perpendicular transport, heat can enter the shadowed flux tube and transport in both directions.

In figure 1(b), the deficiency of the original DFLT method is illustrated. Test particles are initially diffused out of the LCFS into the main channel, with an equal possibility to choose either parallel flow direction, due to the performed two tracings in opposite directions. However, at the downstream

end of the channel far away from the LCFS, all the test particles therein must have passed through the X-point of one island leg, which numerically requires their flow direction to be universally towards the downstream end of the main channel, i.e. towards the left target as shown in the figure. The constant parallel flow direction during the field line tracing prevents DFLT to produce any parallel heat flux at the right target connected with the shadowed flux tube. A finite number of test particles may numerically also hit on the right target, but only due to the randomly large perpendicular displacements, i.e. diffused directly from the main channel.

A new DFLT\_rev method is now proposed in order to compensate for the missing particles on the other side in DFLT. It includes the original DFLT method as the first step and an additional reverse tracing step as the second step. As shown in figure 1(c), in the reverse tracing step all the deposited test particles resulting from both the forward and backward tracings in the DFLT are traced inversely along the field lines in a direction away from the respective PFC surface. The diffusion parameters are kept the same as used in the DFLT for this second step. For the main channel the ratio of test particles deposited at each end remains equal after the reverse tracing step, due to the stellarator symmetry. For the shadowed flux tube, test particles originally deposited only on one end can possibly generate their counterparts on the other end. The heat flux at a certain surface area is finally calculated by counting the sum of hitting events within that area from both the DFLT and the reverse tracing step.

Test particle depositions from the first DFLT step and the second reverse tracing step are presented separately in figure 2 for a better illustration of the DFLT\_rev method. In this example, the typical high-mirror configuration is used. In the first step, namely the DFLT method, all the test particles are diffusively traced in a forward (marked in blue) and a backward direction (marked in red) along the field lines towards the PFCs as shown in figure 2(a). In the second step, all the deposited particles from the first step (re-marked in red) are traced along the field lines away from the PFCs, until a second intersection (marked in blue).

Comparing DFLT\_rev to the original DFLT result, two major differences can be found: (1) the appearance of strong baffle loads on the right side of toroidal angle  $\phi \sim -15.5^\circ$ . (2) The appearance of the middle divertor loads. Notice that a complicated *watershed* is formed in this magnetic configuration at the inner baffle area at  $\phi \sim -15.5^\circ$  [12, figure 8(a) therein], which essentially is the part of the baffle plate designed to protrude towards plasma among surroundings. In the previous study [12], it has been shown that the experimentally observed critical baffle loads reside mainly on the right side of  $-15.5^\circ$ , due to the existence of a shadowed region with long  $L_c$  of  $\sim 32$  m. From the direct comparison between DFLT and DFLT\_rev shown in figure 2, it is obvious that without the reverse tracing step, the loads to the shadowed region including both the inner baffle and the middle divertor part (another shadowed region as will be shown in detail in section 3) can not be properly reproduced.

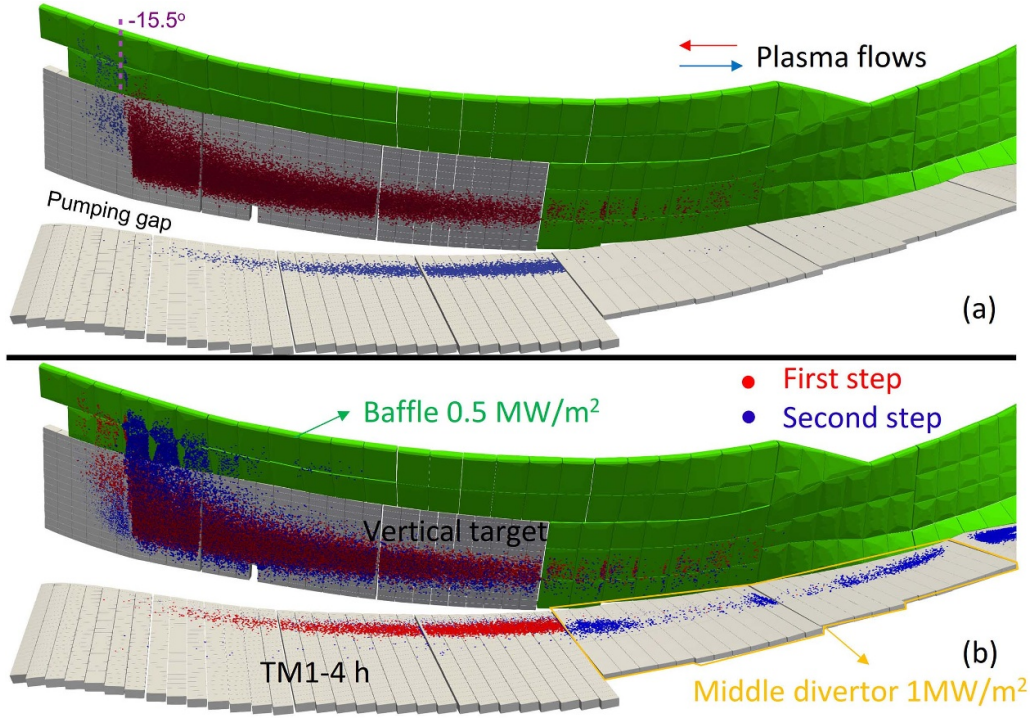


**Figure 2.** Comparisons of the deposited test particles in high-mirror configuration between the DFLT (a) and DFLT\_rev (b) methods. In (a), red points are intersections on the targets resulting from backward tracing with respect to the main field vector, while the blue points are from forward tracing. In (b), the red points are the sum of all the blue and red points in (a), namely the DFLT results, while the blue points are the results of the reverse tracing step from the PFCs.

## 2.2. EMC3-Lite: heat conduction and sheath boundary condition

Aiming for fast estimation of 3D divertor heat loads for future divertor designs, the EMC3-Eirene code has been simplified to EMC3-Lite (details in [20]). It restricts the heat transport equation to only parallel electron conduction and perpendicular heat diffusion terms by neglecting convective heat transport as well as parallel heat conduction of ions:

$$\nabla \cdot (-\kappa_e \nabla_{\parallel} T - \chi n \nabla_{\perp} T) = 0. \quad (1)$$

Here, it has been assumed that electron and ion temperature is equal, i.e.  $T = T_i = T_e$ , and that perpendicular heat diffusion coefficient  $\chi = \chi_e + \chi_i$ . At the target, the Bohm sheath boundary condition holds as

$$-\kappa_e \nabla_{\parallel} T|_{\text{target}} = n C_s \gamma T_r. \quad (2)$$

Here,  $C_s = \sqrt{k(T_{et} + T_{it})/m_i}$ , where  $T_{et}$  and  $T_{it}$  are electron and ion temperature at the target respectively, and  $m_i$  is the ion mass.  $\gamma = \gamma_e + \gamma_i$  is the energy sheath transmission factor, which is assumed to be 7 for W7-X in the code. Further assumption is that electron and ion density are equal for the simulated hydrogen plasma,  $n = n_i = n_e$ , and the electron conductivity is constant, i.e.  $\kappa_e = \kappa_{e0} T_0^{5/2}$ , where  $\kappa_{e0}$  is a physical constant, and  $T_0$  is an input parameter for upstream electron temperature. Such an assumption is valid for low-density plasma where no significant temperature gradient exists from

upstream to downstream. Energy exchanges related to neutral and impurity are completely ignored in EMC3-Lite.

EMC3-Lite is implemented as in EMC3 with the reversible field line mapping numerical method [26], which strongly boosts the calculation speed compared with the traditional FLT method, e.g. Runge–Kutta method. The CPU time spent to generate a typical heat deposition result using EMC3-Lite as will be shown in the next subsection is  $\sim 5$  min, while it requires  $\sim 8$  h for DFLT\_rev to obtain a result with similar statistical quality. All the PFCs are transformed into a so-called Kisslinger's format, where the cylindrical coordinates of the PFC boundaries are stored at each finite step of toroidal angles, e.g. every  $0.5^\circ$  as currently used. Such a format is more suitable in the design phase because the PFC geometry can be more easily modified than the typical triangulation representation. Different from a mimic of reverse flow in DFLT\_rev, the discussed bi-directional heat transport in the shadowed region is naturally established by the sheath boundary condition in EMC3-Lite.

## 2.3. Quantitative comparisons between different models

Heat fluxes can be derived from the scattered deposition points shown in figure 2 using the projection method [6]. The distributions of the power loads resulting from DFLT, DFLT\_rev, and EMC3-Lite respectively are mapped to the same 2D plane for a quantitative comparison as shown in figure 3. The experiment to be compared is 20181009\_009

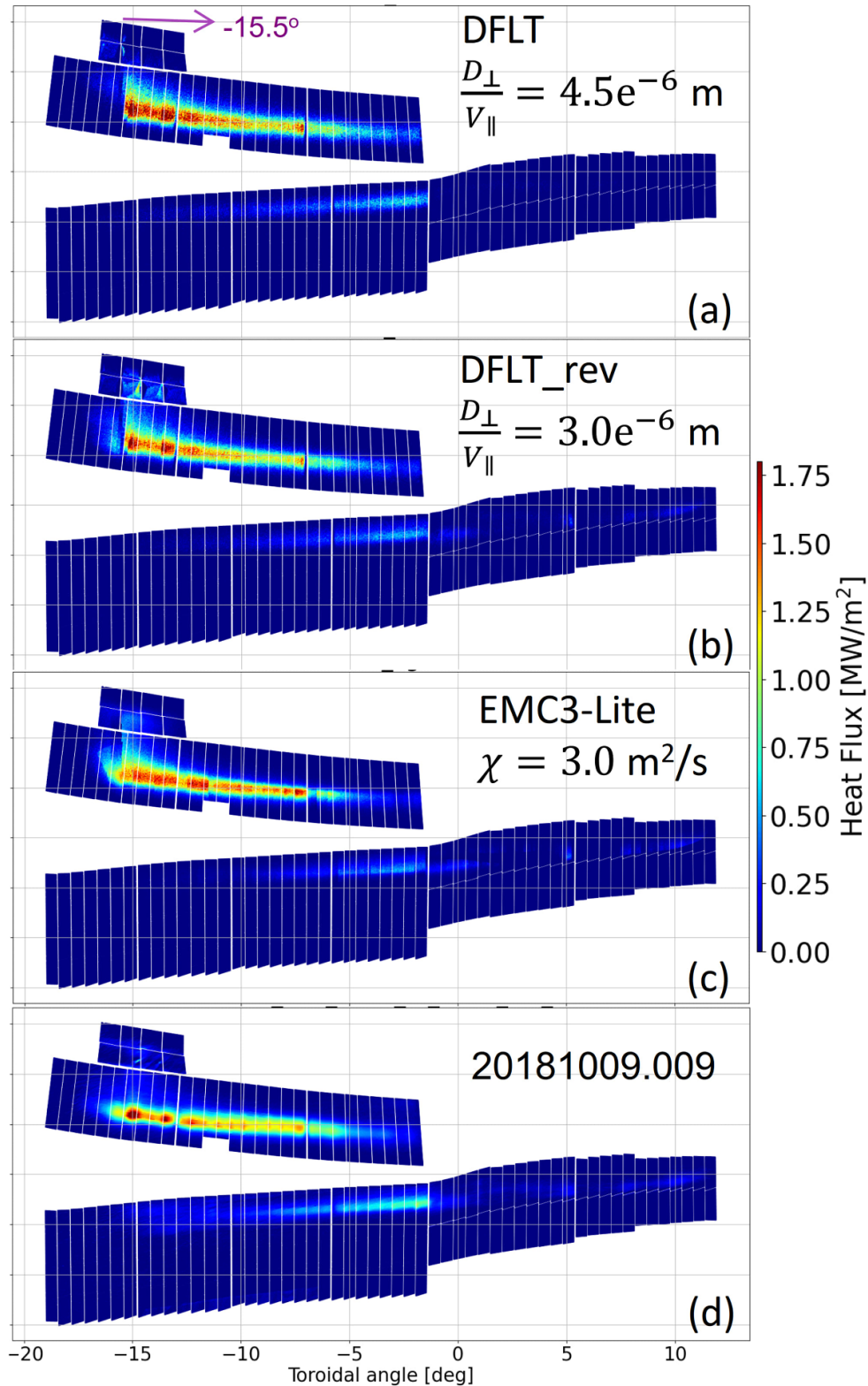


**Figure 3.** Comparison of the simulated heat fluxes among DFLT, DFLT\_rev, EMC3-Lite methods and the averaged experimental result, with different diffusion parameters chosen for each method from fitting the same averaged strike line width of  $\lambda_{\text{int,tar}} \sim 10$  cm on the vertical target.

(for details see section 3), which is in a typical high-mirror configuration. The total input power for all three methods is set to be 1.8 MW, which is consistent with the total divertor heat loads in the experiment calculated by integrating the

heat fluxes on all the divertor units observed by the infrared cameras.

The different diffusion parameters for these methods shown in figure 3 are chosen by fitting the experimental width of the

averaged heat flux profile on the vertical target (shown later in section 3), which is calculated traditionally as the integral power decay length at the target  $\lambda_{\text{int,tar}} = \int_s q(s) ds / q_{\text{max}}$  [27]. All three methods with the respective diffusion parameters fit the experimental value of  $\lambda_{\text{int,tar}} \sim 10$  cm. Interestingly, a lower  $D_{\perp}/v_{\parallel}$  of  $3.0 \times 10^{-6}$  m is found for DFLT\_rev than  $4.5 \times 10^{-6}$  m in DFLT. This may be attributed to the fact that by adding the reverse tracing step in DFLT\_rev, particles travel a longer distance during which diffusion can happen, which as a result requires a relatively lower diffusion coefficient in order to reach the same broadening at the PFCs compared with DFLT.

For EMC3-Lite simulation, the input parameters are  $\chi = \chi_e + \chi_i = 3 \text{ m}^2 \text{ s}^{-1}$ ,  $T_0 = 100 \text{ eV}$ , and  $n = 1 \times 10^{-19} \text{ m}^{-3}$ , which are considered suitable as upstream parameters for such low density plasma. All the input parameters for EMC3-Lite simulations are kept the same for the rest of the paper providing consistency in the simulation environment, such that the studied baffle or middle divertor loads are uniquely influenced by the magnetic topology changes. A perfect match of these upstream parameters to the experimental measurements for each discharge from diagnostics, e.g. Thomson scattering, is difficult to achieve given the accuracy and spatial resolution of the diagnostic at the current stage in the island boundary and is also unnecessary for the purpose of this paper. In a previously studied discharge with similar plasma parameters, an electron temperature of  $\sim 100 \text{ eV}$  was measured using Thomson scattering channels closest to the LCFS, but with a rather large uncertainty [10, figure 2 therein].

From figure 3, it is obvious that the distribution of baffle loads derived from the DFLT method is incorrect. Furthermore, almost no middle divertor heat flux is obtained in the DFLT case. Together with the illustration in section 2.1, it proves again that the experimentally observed baffle and middle divertor loads are dominated by the reverse flow in the shadowed region.

For the peak baffle loads in the DFLT case, one has to be careful that the local hot spot on the corner of one facet at  $\sim -15.5^\circ$  (facet structure see section 4) is caused by heat flux flowing in the forward field direction due to the complicated *watershed* geometry as indicated in figure 2. In other words, the origin of such a very local peak heat load is completely different from the dominant heat load in the shadowed region, which is caused by heat flux flowing in the backward field direction and connects to the 32 m long flux tube with a much broader wetted area covering three tiles of the inner baffle plate. Table 1 compares the results from the three methods to the experiments in terms of the peak ( $q_{\text{peak}}$ ) and averaged heat flux ( $q_{\text{mean}}$ ) at the eight baffle tiles. In DFLT case, the discussed small hot spot generates coincidentally comparable  $q_{\text{peak}}$  as in experiment, while  $q_{\text{mean}}$  is significant lower than experiment by  $\sim 75\%$ .

Different from DFLT, for both DFLT\_rev and EMC3-Lite simulations the location of the main baffle load is reproduced as experimental observation at the correct side of the *watershed*. However, the differences in the amplitude of the

**Table 1.** Comparisons of the averaged and peak heat flux at the 8 baffle tiles shown in figure 3 from different simulation methods and experiment.

	Exp	DFLT	DFLT_rev	EMC3-Lite
$q_{\text{peak}}$ (MW m <sup>-2</sup> )	0.87	0.60	1.42	0.57
$q_{\text{mean}}$ (kW m <sup>-2</sup> )	71.03	17.60	122.25	88.14

baffle heat fluxes among the experimental results, DFLT\_rev, and EMC3-Lite simulations exist and the reason is not yet clear. Specifically, DFLT\_rev shows generally higher heat fluxes than the experiment, while the  $q_{\text{peak}}$  in EMC3-Lite is slightly lower than the experiment as shown in table 1.

A few speculations and discussions could be made for the discrepancies. (a) The experimental results are derived from the averaged heat flux map (see section 3) among eight divertor units available from thermography supervision, i.e. four upper and four lower targets, to compensate for the finite error fields [28, 29] and drifts effects [30]. Through the averaging process, broadening of the loaded area and a reduction of the peak heat flux are inevitable. (b) From the simulation side, Kisslinger's format used in EMC3-Lite has limited resolution in the current version, which results in basically a smooth surface across multiple baffle tiles without any facet structures as exist in the as-built tile surfaces. In DFLT\_rev with a triangulation representation of PFCs, such polygon facets are nevertheless retained with finite tolerances. This difference leads to a higher perpendicular heat flux to the baffle tiles in DFLT\_rev than in EMC3-Lite, i.e.  $q_{\perp,\text{surface}} = q_{\parallel} \sin \alpha$ , due to the larger grazing angle  $\alpha$  between certain baffle facets and the local magnetic field lines. Here,  $q_{\parallel}$  is the parallel heat flux along the local magnetic field line. (c) The missing physics in both models can influence the simulation results, which has been partially confirmed by the complete EMC3-Eirene simulation, including the interaction with impurity and neutrals, and the momentum exchange especially the friction or viscosity between the main heat channel and the shadowed flux tube as discussed previously.

### 3. Control of baffle and middle divertor loads by finite magnetic variations

Detachment has been proved to suppress the convective and conductive power loads to all the PFCs in the standard magnetic configuration in the OP1.2 campaign [10]. To obtain stable detachment in other magnetic configurations, especially high-mirror configuration, with the new water-cooled HHF divertor as well as the cryopump system is one of the main tasks for the upcoming campaign. However, experimental proposals requiring relatively low plasma density and high heating power also exist. Thus, alternative ways rather than detachment should be explored to mitigate the baffle and middle divertor loads, so that the operational window could be expanded in the OP1.2 campaign.

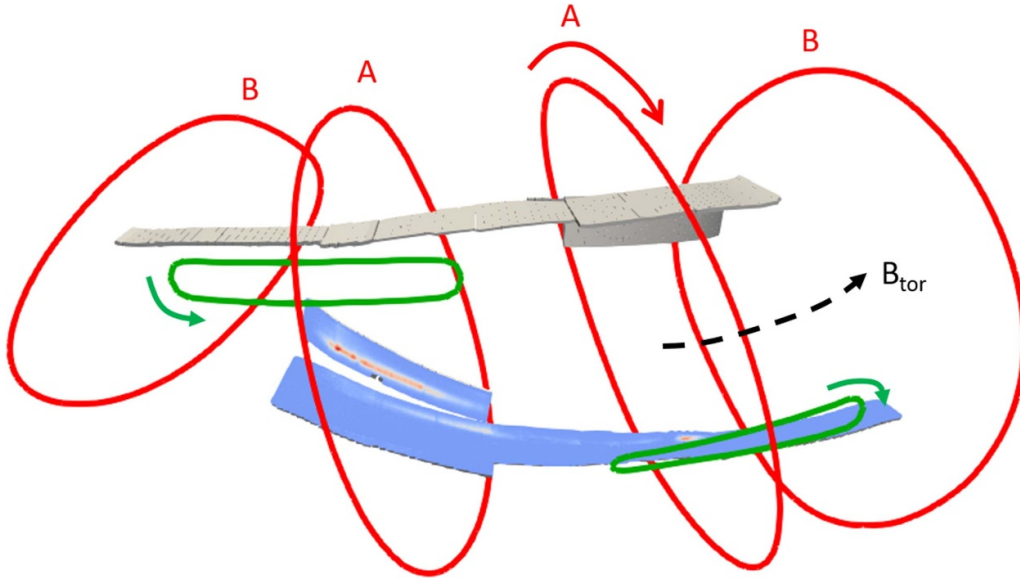


**Figure 4.** Locations of planar coils (both type A and B in red) and control coils (in green) in one machine module, as well as the definition of their positive coil currents indicated by arrows.

Here, we focus on the change of baffle and middle divertor loads induced by tuning of magnetic typologies at the edge by means of control and planar coils [31, figure 1 therein]. In W7-X, the negative planar coil currents in both coil types A and B increase the rotational transform  $\iota = n/m$ , where  $n$  and  $m$  are toroidal and poloidal mode numbers respectively. Such effect has been applied for the  $\iota$  correction experiment [32], and is very similar to the toroidal plasma current effect [33]. In high-mirror and standard magnetic configurations with  $n/m = 5/5$  island chains in the plasma boundary, the two positively charged control coils in each machine module can enlarge the island. In contrast, the negatively charged control coils shrink the island. The location of the relevant coils and the definition of positive coil currents are shown in figure 4.

The main diagnostic used to derive the experimental heat fluxes on the PFCs is the wide-angle infrared thermography systems [6, 34–36]. The averaged heat flux map generated in this section is averaged from both the upper and lower divertor units from machine modules 1 to 4, in order to compensate for the remaining error field [28, 29] and drift effects [30].

### 3.1. Control of baffle loads in high-mirror configuration

High-mirror configuration is optimized for a minimum bootstrap current, a stable field structure against plasma beta effects, and good fast particle confinement, which is also beneficial for NBI operations [31, 37]. However, this configuration is strongly limited in experimental time and plasma parameters in OP1.2 because of the discussed baffle loads [12]. Here, we report on one experimental session in OP1.2 aiming to mitigate the baffle loads by tuning the planar  $I_{A,B}$  and control coil currents  $I_{cc}$ .

Table 2 shows the list of experimental programs and the related settings of the coil currents, which are set identically for all five machine modules. The same plasma parameters

**Table 2.** Coil currents (per winding) used in the experimental programs in high-mirror configurations.

Program	$I_{A,B}$ (A)	$I_{cc}$ (A)
20181009.022	0	1000
20181009.020	0	500
20181009.009	0	0
20181009.015	0	−500
20181009.017	0	−1000
20181009.011	−250	0
20181009.013	−500	0

were intended in these discharges as shown in figure 5, with an input of 3 MW electron cyclotron resonance heating power ( $P_{ECRH}$ ), a controlled plasma line-integrated density ( $\int n dl$ ) of  $\sim 5 \times 10^{19} \text{ m}^{-2}$ , and a measured diamagnetic energy ( $W_{dia}$ ) of  $\sim 0.4 \text{ MJ}$ .

Interestingly, a wide range of the divertor neutral pressure ( $p_{n,div}$ ) from  $1.4 \times 10^{-4} \text{ mbar}$  to  $1.8 \times 10^{-4} \text{ mbar}$  could be measured for these discharges. The higher  $p_{n,div}$  is found to be correlated with the positively charged higher  $I_{cc}$ , which moves the strike line closer to the pumping gap (location marked in figure 2), according to both the simulation and experimental results which will be shown later. However, a lower bound of  $p_{n,div} \sim 1.4 \times 10^{-4} \text{ mbar}$  seems to be present for all the discharges with a negative  $I_{cc}$  or  $I_{A,B}$ . The reason is so far not clear and requires further simulations from EMC3-Eirene including neutral transport for a better understanding.

To explain the  $I_{cc}$  and  $I_{A,B}$  effects on the change of magnetic topology at the island, the  $L_c$  plot overlaid with Poincaré plot at  $\phi = 15^\circ$  for 4 example cases are shown in figure 6. Except for the control of island size, a few quantities can be seen to be inversely proportional to  $I_{cc}$ , including the plasma volume confined within LCFS, the distance between the strike line and

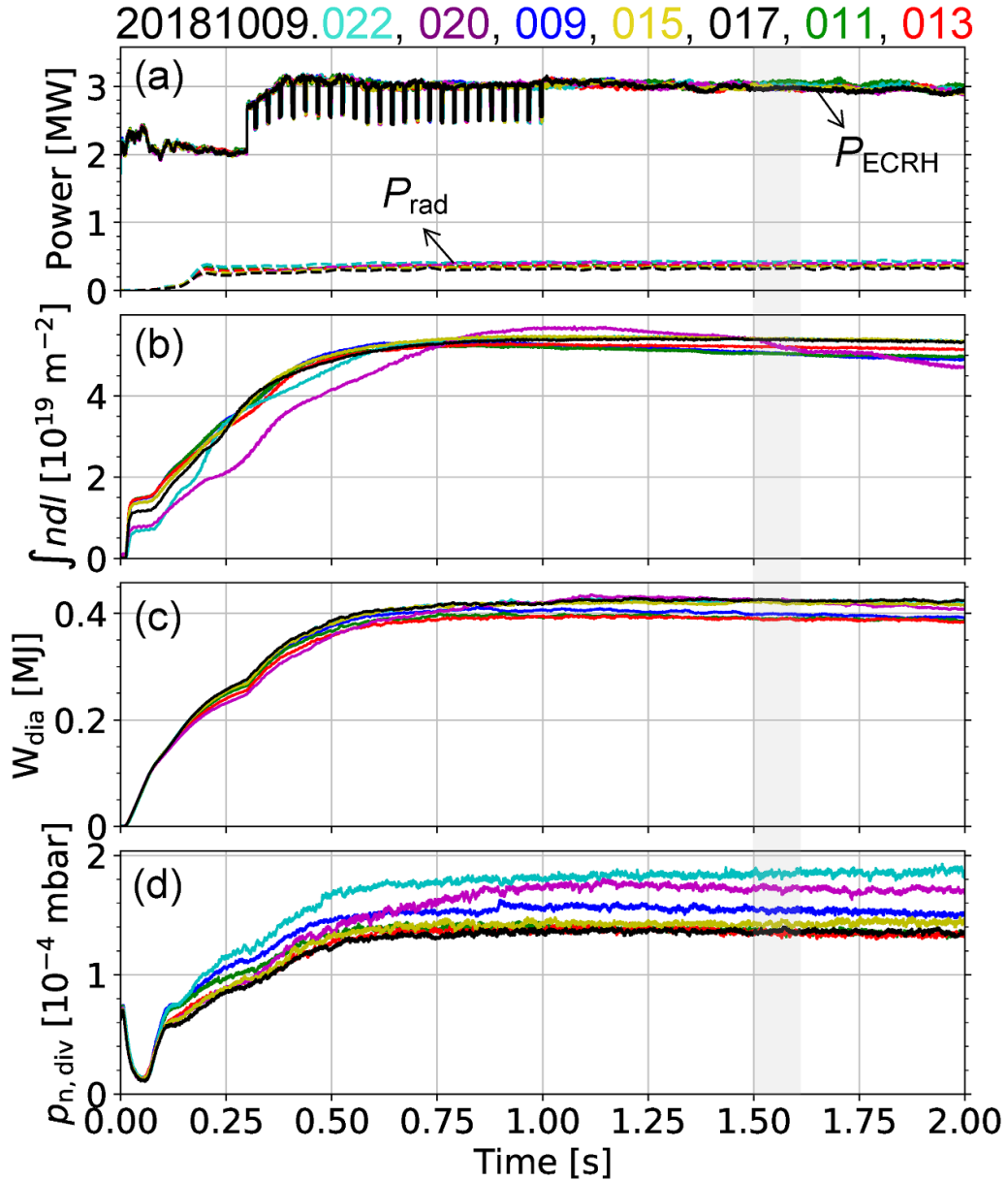


**Figure 5.** Overview of plasma parameters of the experimental programs listed in table 2 in the high-mirror configurations (20181009\_022 (in cyan), 20181009\_020 (in magenta), 20181009\_009 (in blue), 20181009\_015 (in yellow), 20181009\_017 (in black), 20181009\_011 (in green), 20181009\_013 (in red)). (a) ECRH heating power  $P_{\text{ECRH}}$  in solid line and total plasma radiation  $P_{\text{rad}}$  measured by bolometer in dashed line. (b) The line integrated electron density  $\int n_e dl$  measured by the interferometer. (c) The diamagnetic energy  $W_{\text{dia}}$  measured by the in-vessel Rogowski coils. (d) The divertor neutral pressure averaged from the available three pressure gauges close to the divertor pump gap at three different divertor units (AEI30, AEI50 and AEI51) [39, table 1 therein].

the pumping gap, and the  $L_c$  inside the island. With a negative  $I_{A,B} = -500$  A increasing  $t$ , the boundary island is moved towards the magnetic axis, resulting in the appearance of a confined ‘O’ point inside the open island. A smaller plasma volume and a larger displacement of the strike line away from the pumping gap are also followed, as well as an increased  $L_c$  inside the island.

Heat flux maps for different  $I_{cc}$  or  $I_{A,B}$  are compared between experiment and EMC3-Lite simulation in figure 7. Besides the modular averaging, the experimental heat flux map is also averaged over a time window from 1.5 to 1.6 s for a better signal-to-noise ratio. In general, reasonable agreement

between the experimental results and simulations is found with respect to the shape of the thermal footprints on the vertical target and the baffle tiles. Especially, the toroidal extension of the strike line can be reproduced very well, e.g. larger island seems to extend the strike line, while a smaller island or increased  $t$  tends to shorten the toroidal extension of the strike line on the vertical target to different extent. The poloidal width of the strike line is inversely proportional to its toroidal extension, resulting in almost the same integral power loads of  $\sim 1.8$  MW on the divertor for these discharges. Assuming a constant diffusion coefficient  $\chi$  for these discharges, the strike-line width

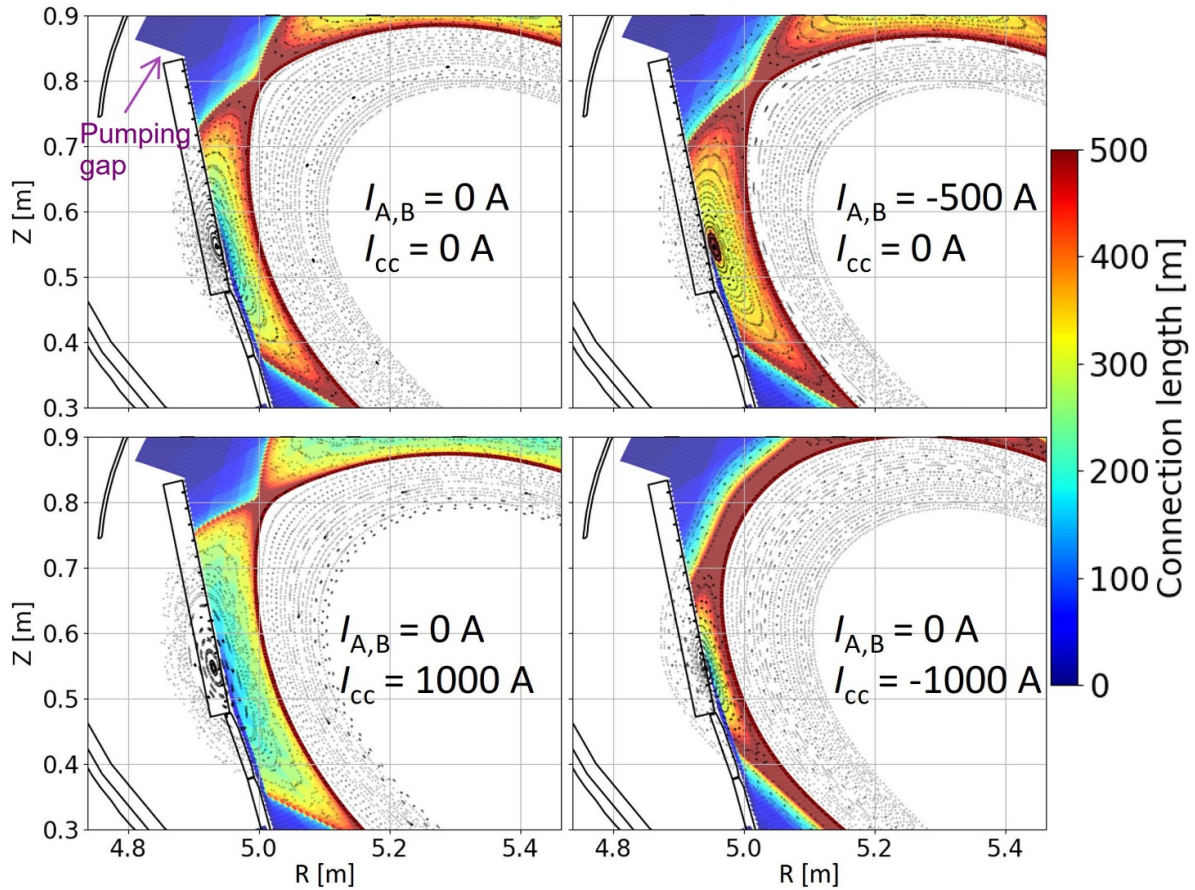


**Figure 6.** Connection length and Poincaré plots for the island intersecting the vertical target at toroidal angle of  $\phi = 15^\circ$  for the four magnetic variants in high-mirror configuration. Notice that this poloidal cross-section is in up-down flip symmetry with the one at  $\phi = -15^\circ$ .

is also as expected to be proportional to  $L_c$ , which is adjusted by coil currents as shown in figure 6.

Although general consistency between EMC3-Lite and the experiment is obtained, differences can still be found. The simulated heat flux patterns are in general smoother than the experiments. The missing hot spots and leading edges at certain locations (e.g.  $-15^\circ$ ) in the EMC3-Lite simulations can be attributed to the simplified representation of the components, with limited toroidal resolution in Kisslinger's format. Further discussions on the discrepancies and the information on the input parameters used for the simulations can be found in section 2.3.

First quantitative comparisons between the EMC3-Lite simulations and the experiments have been made for both the averaged heat flux profile of the vertical target (figure 8) and the maximum heat flux on the eight investigated baffle tiles (figure 9). The simulated strike line location fits very well with the experiment for each case. With regards to the amplitude and the shape of the strike line profile, a perfect match between the experiments and the simulations is not reached and is also not expected. Nevertheless, the difference between simulation and experiment for each case is rather small, even though most of the inputs for the simulation are assumed without careful experimental verification.

Another possible variant in the simulation is the heat diffusion coefficient  $\chi$ , which is assumed to be a constant of  $3 \text{ m}^2 \text{ s}^{-1}$  for all the simulated cases marked with solid lines in figure 8. In order to demonstrate the effect of  $\chi$ , we simulate the  $I_{A,B} = -500 \text{ A}$  case with a doubled  $\chi$  (as shown in dashed cyan line). It can be seen that the peak of the experimental strike line for this case lies in between both simulations.

The critical baffle loads are found to be quite sensitive to the applied coil currents from the first estimation as shown in figure 9. With a change of  $I_{CC}$  from 1 to  $-1 \text{ kA}$ , the maximum baffle heat flux is increased from  $0.6$  to  $1.5 \text{ MW m}^{-2}$ . This suggests that a larger island is beneficial for the shadowing of the baffle components, while a limiter-like variant with a remnant island should be avoided due to the unacceptable baffle loads. With a small offset of  $I_{A,B} = -500 \text{ A}$ , the maximum baffle load increase by  $\sim 40\%$  compared with the no current case. A positive offset of  $I_{A,B}$  has not been tried in OP1.2, which may help to further reduce the baffle loads. However, care should be taken with respect to the associated strike line location that it is unsafe to put heat loads close to the pumping gap.

In general, the simulated maximum baffle load from EMC3-Lite is smaller than the experiment for each case by  $\sim 30\%$ – $40\%$ . However, the trend is very well reproduced, which implies that the change of magnetic topology is the dominant factor responsible for the change of the baffle loads.

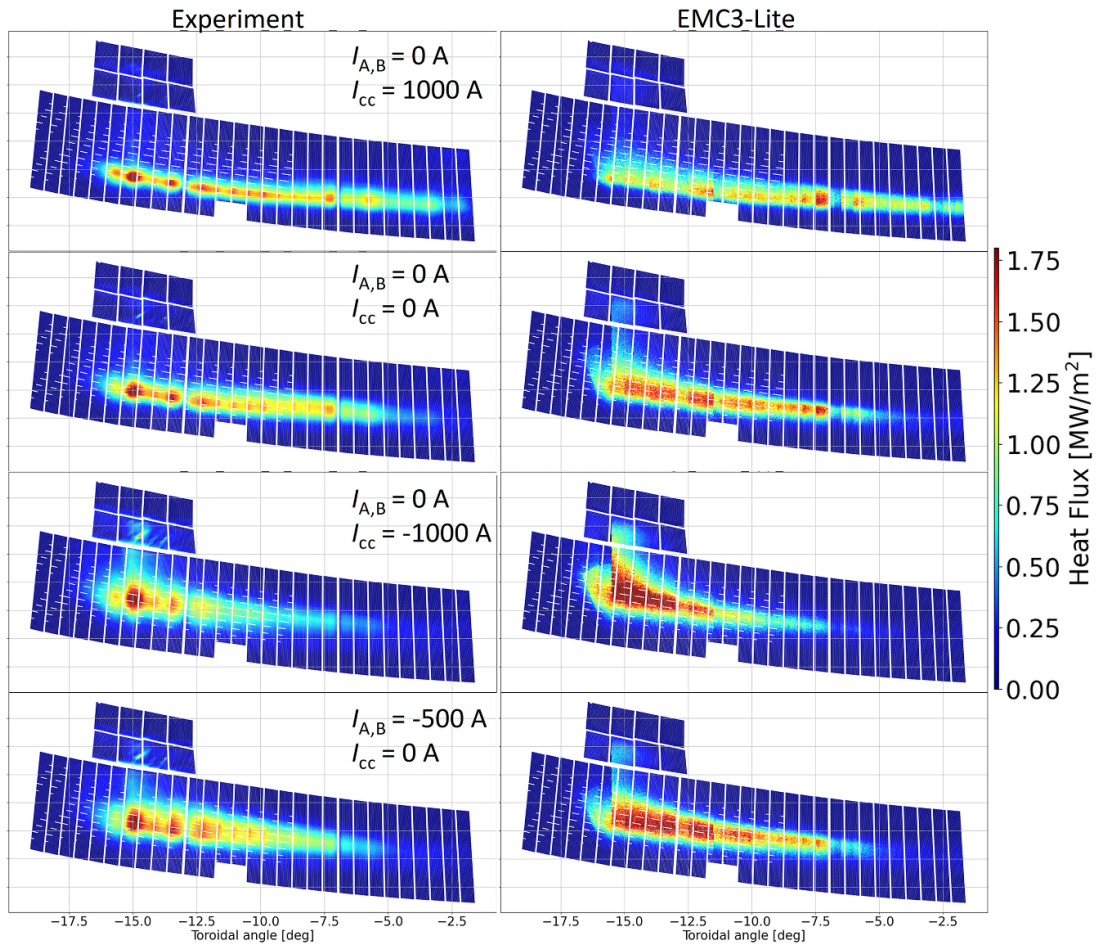


**Figure 7.** Experimental (left column) and simulated (right column) heat flux distributions on the vertical target and the investigated baffle tiles for the four different magnetic variants in high-mirror configurations, i.e. from top to bottom row:  $I_{A,B} = 0$  A and  $I_{cc} = 1000$  A,  $I_{A,B} = 0$  A and  $I_{cc} = 0$  A,  $I_{A,B} = 0$  A and  $I_{cc} = -1000$  A,  $I_{A,B} = -500$  A and  $I_{cc} = 0$  A. The experimental results are averaged over all the available 8 divertor units from machine modules 1 to 4, and also averaged over a time window from 1.5 to 1.6 s.

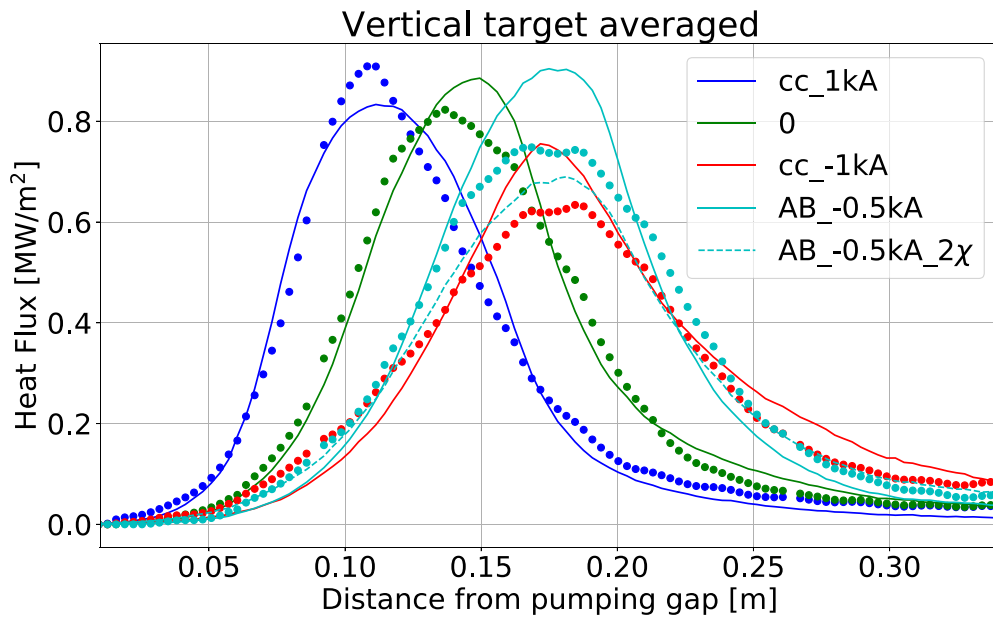


**Figure 8.** Comparison between the experimental (dots) and simulated (solid line) heat flux profile averaged for the entire vertical target for the four magnetic variants in high-mirror configuration, i.e.  $I_{A,B} = 0$  A and  $I_{cc} = 1000$  A in blue,  $I_{A,B} = 0$  A and  $I_{cc} = 0$  A in green,  $I_{A,B} = 0$  A and  $I_{cc} = -1000$  A in red,  $I_{A,B} = -500$  A and  $I_{cc} = 0$  A in cyan. In addition, dashed cyan line shows a simulation result with the same configuration as the last magnetic variant, but with a doubled heat diffusion coefficient than all the others.

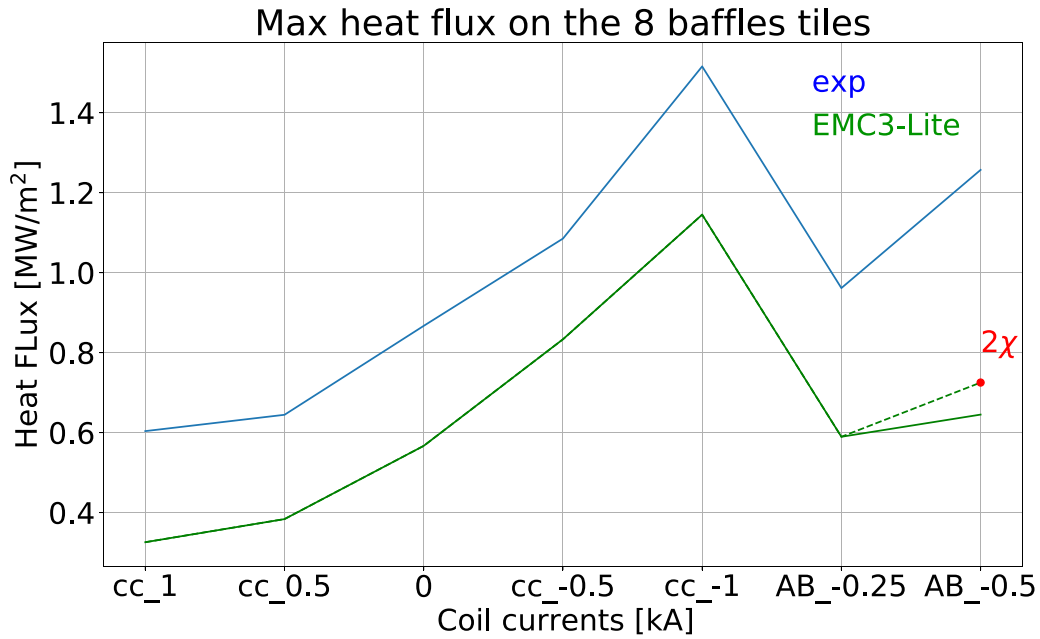


**Figure 9.** Comparison of the maximum heat flux on the eight baffle tiles shown in figure 7 between experiments (in blue) and EMC3-Lite simulations (in green).

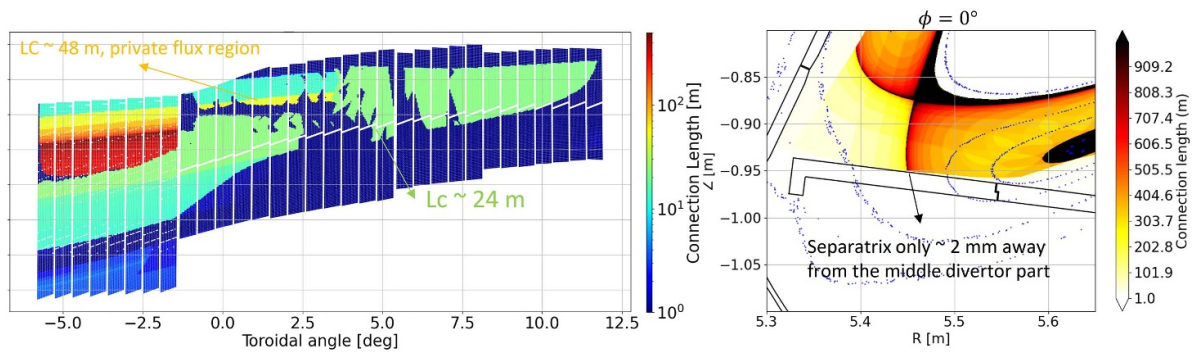


**Figure 10.** Left: The  $L_c$  on the TM4h and middle divertor part in the standard magnetic configuration as applied to discharge 20180905\_015. Right: The  $L_c$  at  $\phi = 0^\circ$  plane in the same magnetic configuration as the left.

A larger perpendicular diffusion is as expected to propagate more energy to the shadowed flux tube, leading to the slightly larger peak baffle load as simulated with the double  $\chi$  case.

### 3.2. Control of middle divertor loads in standard configuration

The middle divertor part was designed to be recessed and shadowed from the nearby divertor modules, with the expected steady-state heat load up to  $1 \text{ MW m}^{-2}$  [13]. However, this limit was frequently reached in high power discharges in OP1.2, especially in standard, low iota, and high iota configurations. We have understood in section 2 that the experimentally observed middle divertor loads are also caused similar to the baffle loads, by the reverse flow in the shadowed region, which is missing in the original DFLT simulation.

The shadowing effect can be seen in figure 10 in standard magnetic configuration, where the  $L_c$  on the entire middle divertor part is calculated to be less than 50 m, which is  $\sim 10$

**Table 3.** Coil currents (per winding) used in experimental programs in standard configurations.

Program	$I_{cc}$ (A)
20180905.011	2000
20180905.014	1000
20180905.015	0

times smaller than the  $L_c$  at the main strike line. However, the distance from the separatrix to the middle divertor part is as small as 2 mm in the poloidal plane. Like the reason for the baffle loads, hot plasma diffusing into shadowed region from the separatrix would flow towards the middle divertor part and leads to potentially an overload.

Comparable discharges in standard configuration with additionally different  $I_{cc}$  are analyzed for the investigation of possible effects of  $I_{cc}$  on the middle divertor loads. The programs are listed in table 3 and the overview plot of plasma

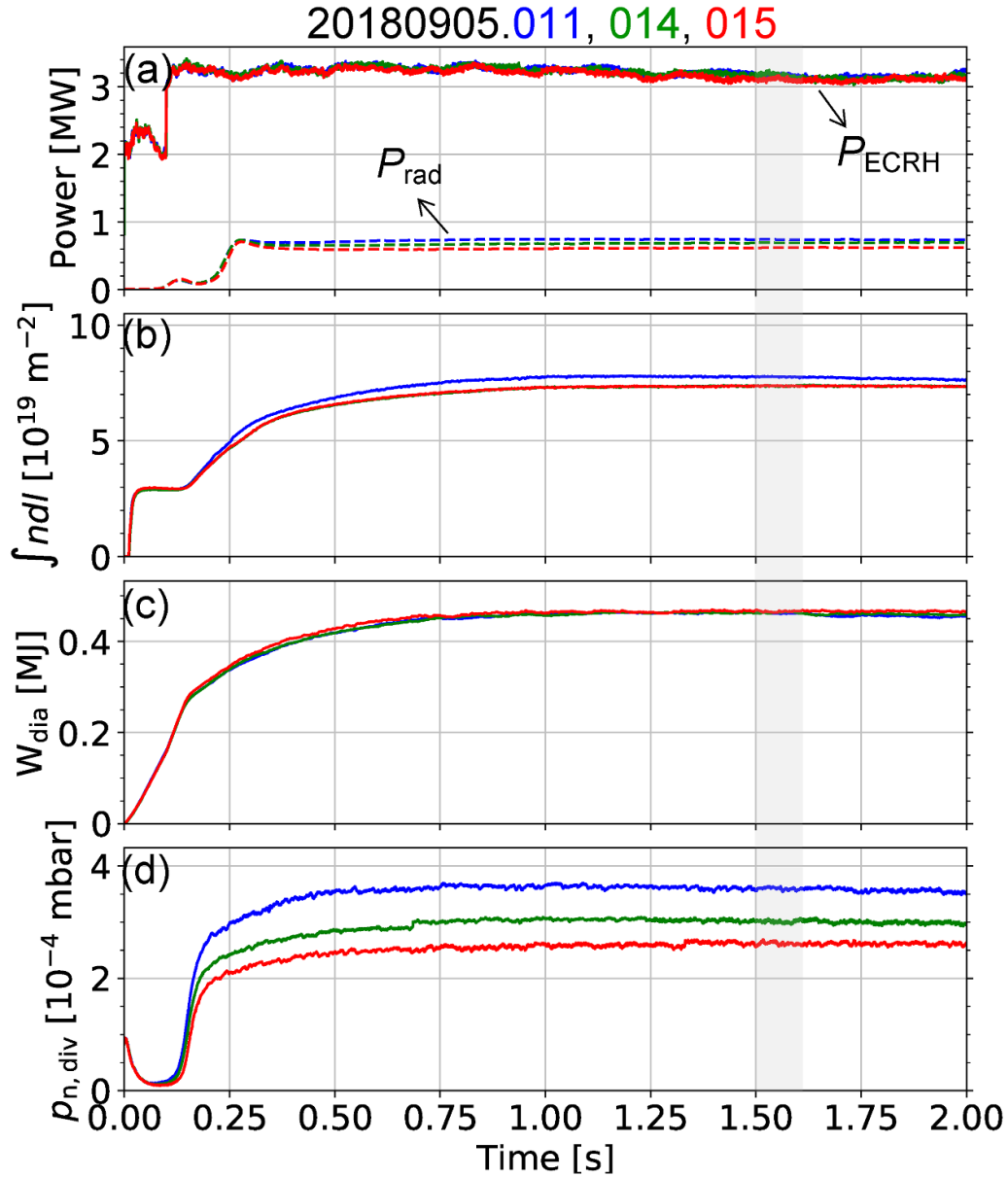
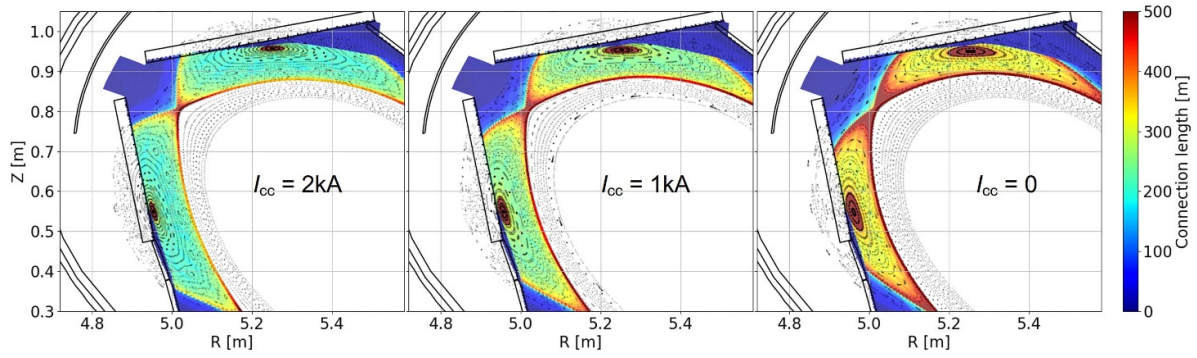


**Figure 11.** Overview of plasma parameters of the experimental programs in the standard configurations with different settings of control coil currents: 20180905\_011 with  $I_{cc} = 2000$  A (in blue), 20180905\_014 with  $I_{cc} = 1000$  A (in green), 20180905\_015 with  $I_{cc} = 0$  A (in red). (a) ECRH heating power  $P_{ECRH}$  in solid line and total plasma radiation  $P_{rad}$  measured by bolometer in dashed line. (b) The line integrated electron density  $\int n_e dl$  measured by the interferometer. (c) The diamagnetic energy  $W_{dia}$  measured by the in-vessel Rogowski coils. (d) The divertor neutral pressure averaged from the available three pressure gauges close to the divertor pump gap at 3 different divertor units (AEI30, AEI50 and AEI51) [39, table 1 therein].

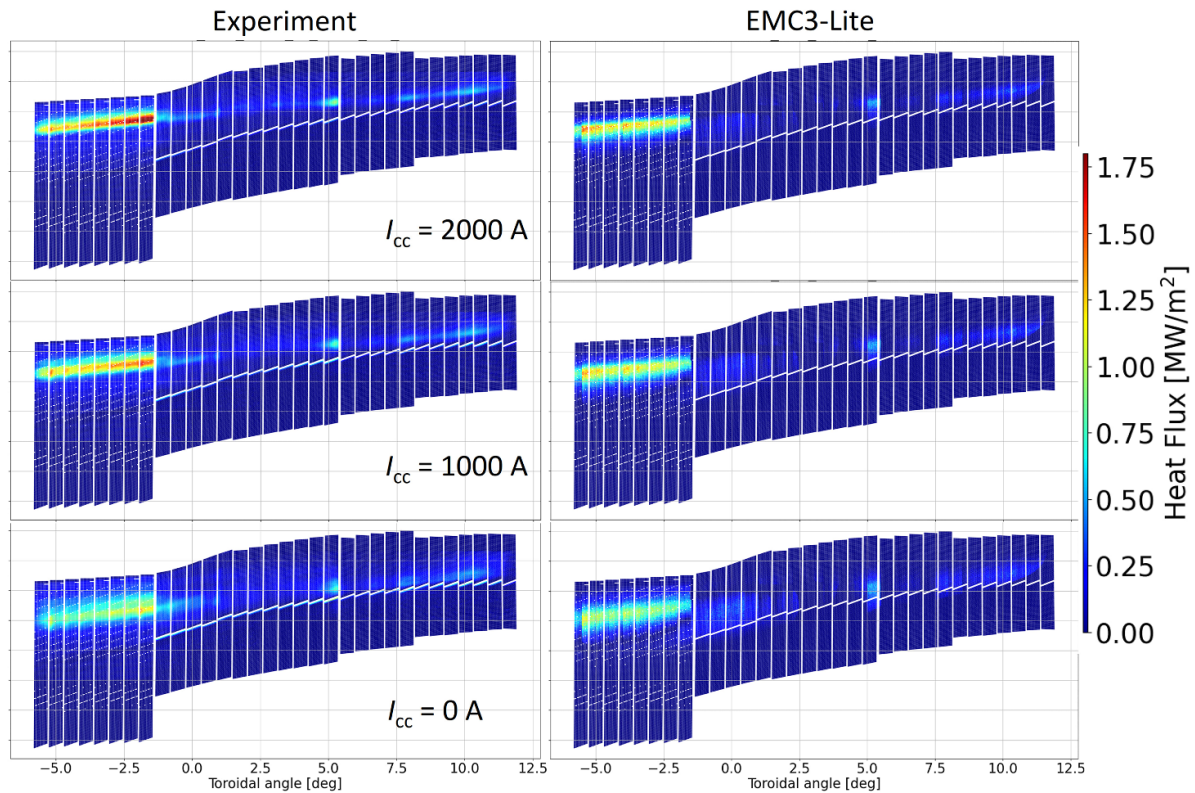
parameters is shown in figure 11. Similar to the high-mirror configuration, the measured divertor neutral pressure  $p_{n,div}$  is strongly correlated with the amplitude of the  $I_{cc}$ . With a 2 kA  $I_{cc}$ , the strike line moves closer to the pumping gap resulting in an increased  $p_{n,div}$  by  $\sim 40\%$ .

Similar effects on the island geometries by  $I_{cc}$  are shown in figure 12 for standard configuration compared with the high-mirror configuration. With an increased  $I_{cc}$ , a larger island, a closer strike line distance to the pumping gap, and a shorter  $L_c$  within the island are obtained. The experimental heat flux

map on the divertor is also compared with EMC3-Lite simulations under different  $I_{cc}$  as presented in figure 13. Here, we focus on the heat distribution on the middle divertor part. A clear hot spot is present and persistent for the different  $I_{cc}$  cases, which is located in between the two divertor modules of the middle divertor part, i.e. at the edge of the last divertor finger of TM5h at  $\phi \sim 5^\circ$ . Except for the hot spot, a discontinuous strike line is also observed to extend toroidally, which is considered to be caused by the perpendicular heat transport from the main heat channel just above the



**Figure 12.** Connection length and Poincaré plots at toroidal angle of  $\phi = 15^\circ$  for the three magnetic variants in standard configuration. From left to right, with  $I_{cc} = 2000$  A,  $I_{cc} = 1000$  A and  $I_{cc} = 0$  A.



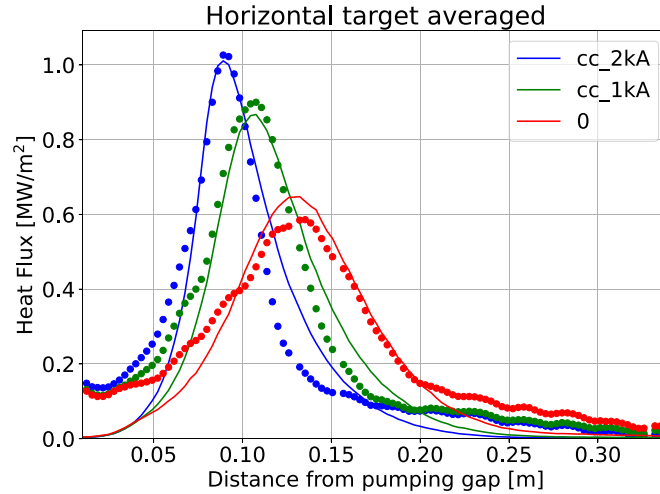
**Figure 13.** Experimental (left column) and simulated (right column) heat flux distributions on the TM4h and the middle divertor part for the three standard magnetic configurations with different control coil currents, i.e. from top to bottom row:  $I_{cc} = 2000$  A,  $I_{cc} = 1000$  A,  $I_{cc} = 0$  A. The experimental results are averaged over all the available 8 divertor units and also averaged over a time window from 1.5 to 1.6 s.

plate in real space. EMC3-Lite reproduces the shape and location of the middle divertor loads, but with reduced amplitude, which is similar to the baffle loads in the high-mirror configuration.

In figure 14, we compare the heat flux profile averaged over the entire horizontal target between the experiment and EMC3-Lite simulation. The dependence of the strike-line location and width on the  $I_{cc}$  is clearly shown in both the experiments and simulations, where a narrower strike line with higher  $I_{cc}$  is due to the reduced  $L_c$  with a larger island. However, elevated heat flux in the private flux region close to the

pumping gap is observed in the experimental profiles, which are not reproduced by the simulations. This mismatch may be attributed to the reduced physics in EMC3-Lite.

Finally, the maximum heat flux on the middle divertor part, i.e. from the hot spot, is compared in figure 15. Due to the already discussed simplified PFC representation, we found in general a smaller peak heat flux in EMC3-Lite compared with the experiment by 25%. With regards to the  $I_{cc}$  effect, according to both the simulation and experiment, the change of the maximum heat flux on the middle divertor part is relatively small. While experimentally an increase of  $I_{cc}$  by 2 kA



**Figure 14.** Comparison between the experimental (dots) and simulated (solid line) heat flux profile averaged for the entire horizontal target for the three discharges in standard magnetic configurations with different control coil currents, i.e.  $I_{cc} = 2000$  A in blue,  $I_{cc} = 1000$  A in green,  $I_{cc} = 0$  A in red.

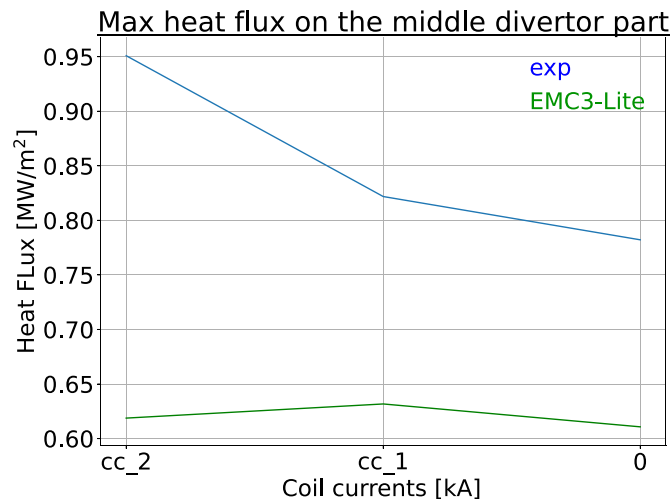


**Figure 15.** Comparison of the maximum heat flux on the middle divertor part between experiments (in blue) and EMC3-Lite simulations (in green).

enhances the peak heat flux by  $\sim 20\%$  on the middle divertor part, in EMC3-Lite the change is rather negligible, for which the reason is not yet clear.

#### 4. New tungsten baffle

The critical graphite baffle tiles receive larger than anticipated heat loads because of the closeness to the main heat channel, long surface  $L_c$ , and large grazing angle [12]. To reduce the baffle loads, a geometric modification has been made to all the 12 baffle tiles in BM1v (the first vertical baffle module to the lower iota end), with the aim to make them smoother and thinner around the *watershed*. Among these optimized baffle tiles, 4 of them, close to the *watershed* are made of tungsten, because the aimed small thickness is below the manufacturing capabilities of graphite due to the relatively lower

mechanical strength. Close to the beam dump area of the neutral beam injection (NBI) system, higher transient shine-through heat loads are expected at the tungsten baffle tiles in module 2 [38]. Therefore, in this machine module for both the upper and lower divertor unit, pure tungsten tiles are used due to its higher thermal limit above  $1200^\circ\text{C}$ , while in other machine modules tungsten-nickel-copper-alloy (95% W, 3.5% Ni, 1.5% Cu) tiles are applied considering better ductile property.

In figure 16, the geometric optimization of BM1v is shown. A retraction of up to  $\sim 7$  mm away from the plasma is achieved around the *watershed* by reducing the tile thickness. The grazing angle between the field line and the surface is also decreased by a factor of 3 at the originally most loaded facet through smoothing. Due to the technical limits of manufacturing, a completely smooth surface as indicated by the dashed line in figure 16(c) is difficult to achieve. Instead, the cross

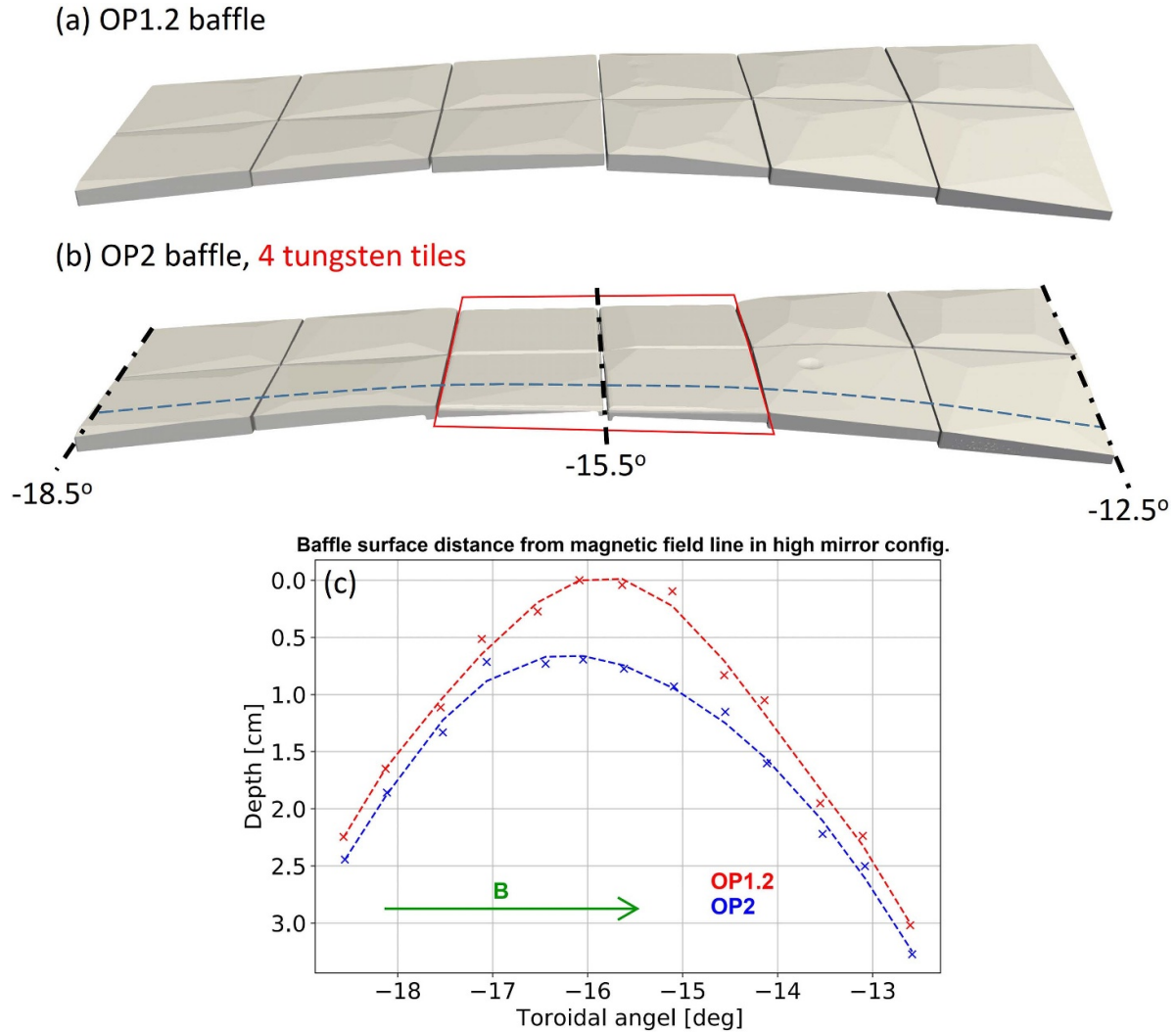


**Figure 16.** Comparison of BM1v baffle structures between OP1.2 (a) and OP2 (b) campaign. (c) Comparison of the distance between the baffle front surface and the plasma at the most critically loaded poloidal location indicated by the dashed blue line in (b) for high-mirror configuration between OP1.2 and OP2 campaigns.

markers show the actual surface of the final design with finite deviation from the dashed line within an acceptable tolerance.

Details on the grazing angle,  $L_c$ , and simulated heat loads for both the OP1.2 and OP2 baffles are compared in figure 17. Here, the grazing angle includes the sign, which implies if the specific field line intersects the surface in a forward field direction (positive sign) or a backward field direction (negative sign). The *watershed* is rather complicated and irregular at the investigated baffle area due to the facets.

With an almost flat surface designed for the new tungsten baffle surface, the originally large grazing angle of  $15^\circ$  at the critical facet has been reduced to within  $5^\circ$ , which significantly mitigates the perpendicular heat flux. From the  $L_c$  plot, it is clear that the same shadowed flux tube with a  $L_c \sim 32$  m is intersected by baffles of both designs, but

with a slightly more even distribution of the intersection area with the OP2 baffle. The heat fluxes are compared between the two designs using the DFLT\_rev method with identical input parameters as used in figure 3(b). The influences of grazing angle and  $L_c$  on the distribution of heat fluxes are obvious and consistent with the previous understanding [12].

Finally, the simulated heat fluxes are quantitatively summarized in table 4, where a benchmark from EMC3-Lite is also included. From both DFLT\_rev and EMC3-Lite methods, a mitigation of both the  $q_{\text{peak}}$  and  $q_{\text{mean}}$  at the 10 baffle tiles by  $\sim 50\%$  is foreseen for the up-coming OP2 campaign. The generally smaller heat fluxes obtained in EMC3-Lite than DFLT\_rev may be due to the missing facets in Kisslinger's format used in EMC3-Lite as discussed in the previous section.

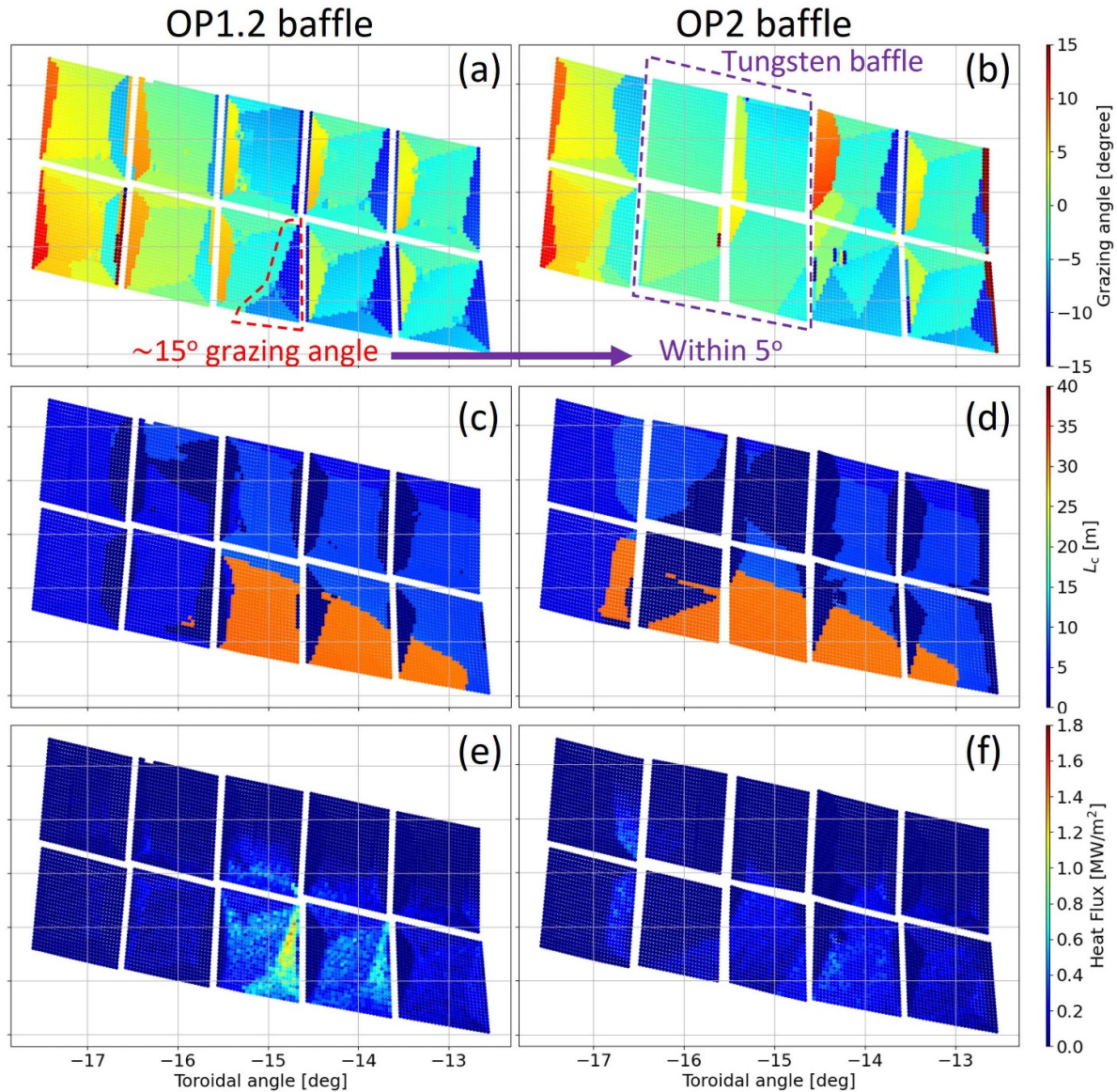


**Figure 17.** Comparison of the grazing angle ((a) and (b)), the connection length  $L_c$  ((c) and (d)) and the simulated heat fluxes from DFLT\_rev ((e) and (f)) between the OP1.2 (left column, i.e. (a), (c) and (e)) and the OP2 baffle tiles (right column, i.e. (b), (d) and (f)).

**Table 4.** Comparisons of the averaged and peak heat flux at the ten baffle tiles as shown in figure 17 between the OP1.2 and OP2 designs using both the DFLT\_rev and EMC3-Lite methods.

	$q_{\text{peak}}$ ( $\text{MW m}^{-2}$ )	$q_{\text{mean}}$ ( $\text{kW m}^{-2}$ )
DFLT_rev OP1.2 baffle	1.42	99.18
DFLT_rev OP2 baffle	0.52	48.87
EMC3-Lite OP1.2 baffle	0.57	74.75
EMC3-Lite OP2 baffle	0.28	32.28

## 5. Conclusion

In the first divertor campaign in Wendelstein 7-X, unexpected overloads at the baffle tiles or at the middle divertor part were frequently observed by the thermography diagnostics, which strongly limited the operational regime in terms of the allowed

maximum heating power and the pulse length. The traditional 3D heat deposition code used for the divertor design in W7-X, the DFLT, failed to reproduce these loads due to the lack of implementation for the bidirectional heat transport in the shadowed flux tubes.

In this paper, after a detailed illustration of the missing physics in DFLT, we introduced two new simulation tools, i.e. DFLT\_rev and EMC3-Lite for the fast and rather accurate estimation of the 3D heat distributions. DFLT\_rev adds a reverse tracing step to DFLT to mimic the originally missing heat flux to the other end of the shadowed flux tube. EMC3-Lite solves the parallel heat conduction with sheath boundary conditions. Both simulations show good agreement with the experiment, especially at the baffle and middle divertor part.

From both experiments and simulations, the baffle load is found to be sensitive to the planar and control coil currents,

while the middle divertor loads are rather persistent regardless of the applied different magnetic variations.

Furthermore, new tungsten baffle tiles have been designed using both the newly proposed codes and mounted on W7-X for the upcoming OP2 campaign. With a retraction and reshaping of the tile surfaces, a 50% mitigation of the baffle load is anticipated.

EMC3-Lite is proved to be a reliable and efficient tool for predicting heat distributions on the PFCs in 3D devices, especially valuable for the design and optimization of PFCs, given the enormously reduced CPU calculation time by a factor of 100 compared with DFLT\_rev.

## Acknowledgments

This work has been carried out within the framework of the EUROfusion Consortium, funded by the European Union via the Euratom Research and Training Programme (Grant Agreement No. 101052200—EUROfusion). Views and opinions expressed are however those of the author(s) only and do not necessarily reflect those of the European Union or the European Commission. Neither the European Union nor the European Commission can be held responsible for them.

## ORCID iDs

Yu Gao  <https://orcid.org/0000-0001-8576-0970>  
 Yuhe Feng  <https://orcid.org/0000-0002-3846-4279>  
 Michael Endler  <https://orcid.org/0000-0003-2314-8393>  
 Marcin W. Jakubowski  <https://orcid.org/0000-0002-6557-3497>  
 Sergey Bozhenkov  <https://orcid.org/0000-0003-4289-3532>  
 Fabio Pisano  <https://orcid.org/0000-0003-0162-0562>  
 Daihong Zhang  <https://orcid.org/0000-0002-5800-4907>  
 Georg Schlisio  <https://orcid.org/0000-0002-5430-0645>  
 Uwe Wenzel  <https://orcid.org/0000-0002-4107-9291>  
 Thomas Sunn Pedersen  <https://orcid.org/0000-0002-9720-1276>

## References

- [1] Feng Y., Kobayashi M., Lunt T. and Reiter D. 2011 Comparison between stellarator and tokamak divertor transport *Plasma Phys. Control. Fusion* **53** 024009
- [2] Pedersen T.S. et al 2018 First results from divertor operation in Wendelstein 7-X *Plasma Phys. Control. Fusion* **61** 014035
- [3] Klinger T. et al 2019 Overview of first Wendelstein 7-X high-performance operation *Nucl. Fusion* **59** 112004
- [4] Wolf R.C. et al 2019 Performance of Wendelstein 7-X stellarator plasmas during the first divertor operation phase *Phys. Plasmas* **26** 082504
- [5] Pedersen T.S. et al 2019 First divertor physics studies in Wendelstein 7-X *Nucl. Fusion* **59** 096014
- [6] Gao Y., Jakubowski M.W., Drewelow P., Pisano F., Puig Sitjes A., Niemann H., Ali A. and Cannas B. 2019 Methods for quantitative study of divertor heat loads on W7-X *Nucl. Fusion* **59** 066007
- [7] Zhang D. et al 2019 First observation of a stable highly dissipative divertor plasma regime on the Wendelstein 7-X stellarator *Phys. Rev. Lett.* **123** 025002
- [8] Effenberg F. et al 2019 First demonstration of radiative power exhaust with impurity seeding in the island divertor at Wendelstein 7-X *Nucl. Fusion* **59** 106020
- [9] Schmitz O. et al (The W7-X Team) 2021 Stable heat and particle flux detachment with efficient particle exhaust in the island divertor of Wendelstein 7-X *Nucl. Fusion* **61** 016026
- [10] Feng Y. et al 2021 Understanding detachment of the W7-X island divertor *Nucl. Fusion* **61** 086012
- [11] Jakubowski M. et al 2021 Overview of the results from divertor experiments with attached and detached plasmas at Wendelstein 7-X and their implications for steady-state operation *Nucl. Fusion* **61** 106003
- [12] Gao Y. et al 2020 Understanding baffle overloads observed in high-mirror configuration on Wendelstein 7-X *Nucl. Fusion* **60** 096012
- [13] Peacock A. et al 2014 Status of high heat flux components at W7-X *IEEE Trans. Plasma Sci.* **42** 524
- [14] Wang Z., Boscary J. and Schauer F. 2020 Thermal and mechanical analyses of W7-X plasma facing components for operation phase 2 *Fusion Eng. Des.* **161** 111882
- [15] Feng Y., Sardei F., Grigull P., McCormick K., Kisslinger J. and Reiter D. 2006 Physics of island divertors as highlighted by the example of W7-AS *Nucl. Fusion* **46** 807
- [16] Bozhenkov S., Geiger J., Grahl M., Kißlinger J., Werner A. and Wolf R.C. 2013 Service oriented architecture for scientific analysis at W7-X. An example of a field line tracer *Fusion Eng. Des.* **88** 2997
- [17] Feng Y., Sardei F., Kisslinger J., Grigull P., McCormick K. and Reiter D. 2004 3D edge modeling and island divertor physics *Contrib. Plasma Phys.* **44** 57
- [18] Reiter D., Baelmans M. and Börner P. 2005 The EIRENE and B2-EIRENE codes *Fusion Sci. Technol.* **47** 172
- [19] Knieps A. et al 2022 Anisotropic diffusion as a proxy model for the estimation of heat-loads on plasma-facing components *Plasma Phys. Control. Fusion* **64** 084001
- [20] Feng Y. (W7-X-Team) 2022 Review of magnetic islands from the divertor perspective and a simplified heat transport model for the island divertor *Plasma Phys. Control. Fusion* **64** 125012
- [21] Kisslinger J. et al 1994 Island divertor for the stellarator Wendelstein 7-X *21st EPS Conf. on Controlled Fusion and Plasma Physics* (European Physical Society) pp 368–71 (available at: [http://libero.ipp.mpg.de/libero/PDF/EPS\\_21\\_Vol1\\_1994.pdf](http://libero.ipp.mpg.de/libero/PDF/EPS_21_Vol1_1994.pdf)) Montpellier, France 27 June - 1 July 1994
- [22] Lore J.D., Cianciosa M., Frerichs H., Geiger J., Hoelbe H. and Boscary J. 2018 Modeling and preparation for experimental testing of heat fluxes on W7-X divertor scraper elements *IEEE Trans. Plasma Sci.* **46** 1387
- [23] Lore J. et al 2019 Measurement and modeling of magnetic configurations to mimic overload scenarios in the W7-X stellarator *Nucl. Fusion* **59** 066041
- [24] Perseo V., Effenberg F., Gradic D., König R., Ford O.P., Reimold F., Ennis D.A., Schmitz O. and Sunn Pedersen T. 2019 Direct measurements of counter-streaming flows in a low-shear stellarator magnetic island topology *Nucl. Fusion* **59** 124003
- [25] Stangeby P. 2000 *The Plasma Boundary of Magnetic Fusion Devices* (Bristol: Institute of Physics Publishing, Nicki Dennis)
- [26] Feng Y., Sardei F. and Kisslinger J. 2005 A simple highly accurate field-line mapping technique for three-dimensional Monte Carlo modeling of plasma edge transport *Phys. Plasmas* **12** 052505

- [27] Loarte A. *et al* 1999 Multi-machine scaling of the divertor peak heat flux and width for L-mode and H-mode discharges *J. Nucl. Mater.* **266** 587
- [28] Bozhnikov S., Otte M., Biedermann C., Jakubowski M., Lazerson S.A., Sunn Pedersen T. and Wolf R.C. 2018 Measurements and correction of the 1/1 error field in Wendelstein 7-X *Nucl. Fusion* **59** 026004
- [29] Lazerson S.A. *et al* 2018 Error fields in the Wendelstein 7-X stellarator *Plasma Phys. Control. Fusion* **60** 124002
- [30] Hammond K.C. *et al* 2019 Drift effects on W7-X divertor heat and particle fluxes *Plasma Phys. Control. Fusion* **61** 125001
- [31] Geiger J., Beidler C.D., Feng Y., Maaßberg H., Marushchenko N.B. and Turkin Y. 2014 Physics in the magnetic configuration space of W7-X *Plasma Phys. Control. Fusion* **57** 014004
- [32] Lazerson S.A. *et al* 2019 Tuning of the rotational transform in Wendelstein 7-X *Nucl. Fusion* **59** 126004
- [33] Gao Y. *et al* 2019 Effects of toroidal plasma current on divertor power depositions on Wendelstein 7-X *Nucl. Fusion* **59** 106015
- [34] Jakubowski M. *et al* 2018 Infrared imaging systems for wall protection in the W7-X stellarator (invited) *Rev. Sci. Instrum.* **89** 10E116
- [35] Puig Sitjes A. *et al* 2018 Wendelstein 7-X near real-time image diagnostic system for plasma-facing components protection *Fusion Sci. Technol.* **74** 116
- [36] Pisano F., Cannas B., Jakubowski M.W., Niemann H., Puig Sitjes A. and Wurden G.A. 2018 Towards a new image processing system at Wendelstein 7-X: from spatial calibration to characterization of thermal events *Rev. Sci. Instrum.* **89** 123503
- [37] Äkäslompolo S., Drevlak M., Turkin Y., Bozhnikov S., Jesche T., Kontula J., Kurki-Suonio T. and Wolf R.C. 2018 Modelling of NBI ion wall loads in the W7-X stellarator *Nucl. Fusion* **58** 082010
- [38] Äkäslompolo S. *et al* 2019 Armoring of the Wendelstein 7-X divertor-observation immersion-tubes based on NBI fast-ion simulations *Fusion Eng. Des.* **146** 862
- [39] Wenzel U. *et al* 2022 Gas exhaust in the Wendelstein 7-X stellarator during the first divertor operation *Nucl. Fusion* **62** 096016